AIAA JOURNAL
Vol. 44, No. 12, December 2006

Steady Flows in the Slender, Noncircular, Combustion Chambers of Solid Propellant Rockets

Vadim N. Kurdyumov*
CIEMAT, 28040 Madrid, Spain

DOI: 10.2514/1.21125

An analysis of the steady flows with axial vortices in slender, cylindrical, nonaxisymmetric cavities generated by injection from their porous walls is presented. This problem is encountered in the description of the flow in slender combustion chambers of solid-propellant rocket motors associated with the gasification of the solid propellant surrounding the combustion chamber. Nonreacting flow can be described in terms of self-similar solutions of the Navier–Stokes equations and the solution, calculated numerically for noncircular grain configurations, shows strong axial vortices, with a viscous vortex core that has been analyzed asymptotically for large Reynolds numbers. It was found that the important property of the flow, namely, $C^{1/2}S/\Pi$, where C is a constant determining the axial pressure gradient, S and Π are the cross section area and its perimeter, respectively, becomes unexpectedly close to $\pi/2$ at large Reynolds numbers, independently on the geometry of the cross section of the cavity. One can suppose that $C^{1/2}S/\Pi = \pi/2$ for any cavities in the invicsid limit, a conjecture that also obtained a support from numerical calculations of flows in rectangular cavities generated by injection from their porous walls.

I. Introduction

THE gasification and combustion of the solid propellant lining inside a rocket chamber takes place in a thin reaction layer adjacent to the gas–solid interface. The gas produced as a consequence of these processes is seen to be emerging from the solid surface normally, with a constant temperature and velocity small compared to the sound velocity. The resulting flowfield is encountered in many other interior flows in cavities generated by a flux from porous walls bounding the cavity. They have received attention in the literature, but not for cavities with more complex cross sections than a circular one or a two-dimensional channel, with the exception of Balachandar et al. [1], despite the role these flows play in solid-propellant rocket motors.

The earliest studies of steady flows of a viscous incompressible fluid driven by uniform injection from porous walls can be traced back to Berman [2]. Taylor [3] showed, in a pioneering work, that the flows generated by injection from the boundary are rotational, even in the inviscid limit, because the boundary layer is blown off, and they must satisfy the nonslip conditions at the boundary. Proudman [4] investigated flows in a two-dimensional channel in the limit of large cross-flow Reynolds numbers and constructed the general inviscid solution. Culick [5] constructed the inviscid solution for axisymmetric flow in a slender chamber of circular cross-section. These results are based on the assumption of self-similarity of the solution with respect to the axial distance z to the closed wall. As shown by Balakrishnan et al. [6], the ratio of the characteristic dimension a of the cross section of the cavity to the chamber length L must be small, $a/L \ll 1$, for the self-similar description to apply. Even in this case the self-similarity breaks down at distances to the end wall of order a, because the boundary layer due to the radial flow on the end wall separates leading to a recirculation bubble attached to the end wall, as seen clearly in the experiments of Dunlap et al. [7]. The self-similarity will also be lost in another region scaled with a, close to the nozzle. The viscous flow models that incorporate also the effect of wall regression were considered by Majdalani et al. [8] and Dauenhauer and Majdalani [9]. The stability analyses of the self-similar flows were carried out recently by Griffond et al. [10], Griffond and Casalis [11], and Chedevergne et al. [12].

In practice the cross sections of the solid propellant chambers are seldom circular and often star-shaped; see Sutton and Biblarz [13]. The flow involves longitudinal, in additional to the transverse, vorticity. The first attempt to describe the axial vorticity has been carried out by Balachandar et al. [1], where small perturbations of Culick's solution were considered. Their linear analysis is valid if $\varepsilon Re \ll 1$, where ε measures the perturbation in the radius of the cavity and Re is an Reynolds number based on the effective gasification velocity and chamber radius. The authors of Balachandar et al. [1] came to the conclusion that modest deviations from the symmetry can have profound effects on the nature of the flowfield.

The purpose of this paper is to contribute to the description of the flows inside noncircular cylindrical cavities, shown in the sketch of Fig. 1, when the deviations from circular cross section are not small. Some numerical results about such flows were presented recently in Liñán et al. [14], together with the analysis of the Euler equations. The present paper is structured as follows. The formulation focussed on the self-similar flows is presented in Sec. II. Section III describes the method of potential–solenoidal decomposition applied to calculate the flowfield numerically, giving in Sec. IV some representative cases. Section V is devoted to the asymptotic description of the viscous core of the vortices appearing away from the center of chamber that has been carried out for Reynolds numbers of the transverse flow larger compared to unity. Some final comments are given in Sec. VI.

II. General Formulation

Consider a rocket motor chamber lined inside with a solid propellant, as sketched in Fig. 1. Two important assumptions have been used in this study to facilitate the description of the steady flowfield inside the chamber, in first approximation. The first one is concerned with the disparity between the density of the gas produced by combustion processes in the neighborhood of the solid surface and the density of the solid propellant leading to a negligible ratio of the regression velocity of the propellant surface to the normal gas velocity. Thus, the flow is modeled by the flow injection from a fixed surface with a constant wall-normal injection velocity U_n.

The second assumption is justified by a small value of the typical ratio of the throat area of the nozzle attached to the chamber exit and the internal area of the chamber. Even though the Mach number in the

Received 14 November 2005; revision received 21 August 2006; accepted for publication 14 September 2006.

*División de Combustión y Gasificación, Avda. Complutense 22; vadim.k@ciemat.es.

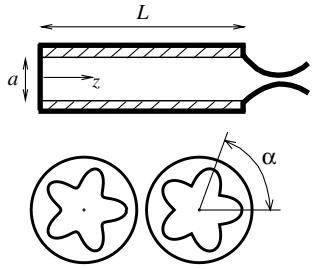

Fig. 1 Sketch of the problem with smooth and nonsmooth shapes of the cross section area.

nozzle throat is close to unity, the value of the Mach number in the chamber remains small from mass conservation considerations. Then, the gas flow in the chamber is described by the incompressible Navier–Stokes equations with a constant density ρ and a kinematic viscosity ν. It should be noted that for very long chambers the compressibility effects could be not negligible near the end of the chamber, before the nozzle.

The analysis carried out in the paper is confined to slender chambers with cylindrical cavities of noncircular cross sections with a transverse characteristic size a small compared to the chamber length L, as is shown in Fig. 1. If we place the origin of the cylindrical coordinate system, (r, φ, z), in the center point of the chamber bottom, the cross section shape of the chamber is given by $r = R(\varphi)$. Function $R(\varphi)$ is assumed to be 1) a α-periodic function of the azimuthal angle φ, where $\alpha = 2\pi/N$ and N is an integer number; and 2) a symmetric function with respect to $\varphi = \alpha/2$ in the interval $0 \le \varphi \le \alpha$ having the maximum and minimum values at $\varphi = 0$ and $\varphi = \alpha/2$, respectively. In the present study we consider that $R^I(0) = 0$, but the value of $R^I(\alpha/2)$ may be both zero and nonzero, describing the shapes with smooth and nonsmooth corners at $\varphi = \alpha/2$, respectively, as shown in Fig. 1.

The dimensional perimeter of the cross section area is $\Pi' = \int_0^{2\pi} \sqrt{R^2 + R^{I2}}\, \mathrm{d}\varphi$. The value $r_c = \Pi'/2\pi$ (which is of order a) is used later to measure the spatial coordinates, whereas U_n and ρU_n^2 are used as scales for velocities and pressure, respectively.

We seek in this study the steady solutions of the governing equations. In the region near the chamber bottom, $z \sim \mathcal{O}(1)$, the flowfield is three-dimensional, except for the case of the circular cross section, $R = \text{const}$, when the flowfield becomes independent on the azimuthal coordinate φ. Nevertheless, far from the chamber bottom, at $z \gg 1$, the steady Navier–Stokes equations have a separable solution of the form

$$v_r = v_r(r, \varphi), \qquad v_\varphi = v_\varphi(r, \varphi), \qquad v_z = zW(r, \varphi)$$
$$P = -\frac{1}{2} C z^2 + p(r, \varphi) \tag{1}$$

where C is an unknown beforehand constant, to be determined as a part of the solution. In fact, form (1) of the solution corresponds to a first term of an expansion in powers of the ratio $a/L \ll 1$.

Substituting (1) into the steady Navier–Stokes equations reduces the problem to the following form:

$$(\nabla \cdot \boldsymbol{v}) + W = 0 \tag{2}$$

$$(\boldsymbol{v} \cdot \nabla)\boldsymbol{v} = -\nabla p + Re^{-1} \Delta \boldsymbol{v} \tag{3}$$

$$(\boldsymbol{v} \cdot \nabla) W + W^2 = C + Re^{-1} \Delta W \tag{4}$$

where $Re = U_n r_c/\nu$ is the Reynolds number, $\boldsymbol{v} = (v_r, v_\varphi)$ is the projection of the velocity vector on the transverse plane, and the conventional operators ∇ and Δ depend on r and φ only.

In the frame of preceding approximations, the boundary conditions at the chamber surface become

$$r = R(\varphi)\text{: } W = 0, \qquad (\boldsymbol{v} \cdot \boldsymbol{n}) = 1, \qquad (\boldsymbol{v} \cdot \boldsymbol{t}) = 0 \tag{5}$$

where

$$\boldsymbol{n} = \left(\frac{-1}{\sqrt{1 + (R^I/R)^2}}, \frac{R^I/R}{\sqrt{1 + (R^I/R)^2}} \right)$$
$$\boldsymbol{t} = \left(\frac{R^I/R}{\sqrt{1 + (R^I/R)^2}}, \frac{1}{\sqrt{1 + (R^I/R)^2}} \right) \tag{6}$$

are the inner normal and tangential unit vectors to the chamber surface, respectively.

It is assumed that the solutions are symmetric about $\varphi = 0$ and $\varphi = \alpha/2$, reducing the domain to solve Eqs. (2–4) to the half of the sector, $0 < \varphi < \alpha/2$. The radial velocity, pressure, and the axial velocity gradient W are symmetric and v_φ is antisymmetric about $\varphi = 0$ and $\varphi = \alpha/2$:

$$\frac{\partial v_r}{\partial \varphi} = \frac{\partial p}{\partial \varphi} = \frac{\partial W}{\partial \varphi} = v_\varphi = 0 \tag{7}$$

The two-dimensional stream function corresponding to transverse flow $\boldsymbol{v}$ cannot be introduced directly, but we will use next the streamlines satisfied the equation

$$\frac{\mathrm{d}r}{v_r} = \frac{r\, \mathrm{d}\varphi}{v_\varphi} \tag{8}$$

In the case of the circular cross section, the inviscid solution of problem (2–5), first obtained by Culick [5], takes the form

$$v_r = -r^{-1} \sin(\pi r^2/2), \qquad v_\varphi = 0, \qquad W = \pi \cos(\pi r^2/2)$$
$$C = \pi^2 \tag{9}$$

The numerical solutions for finite Reynolds numbers in this case, including the very small and very large values of Re, were given recently in Balachandar et al. [1], where the main objective was to study the influence of the small deviations of the cross section shape from the circular one on the flow.

III. Potential–Solenoidal Decomposition

Following a theorem of vector geometry that a vector field may be decomposed into potential and solenoidal parts, we write the transverse velocity in the form $\boldsymbol{v} = \nabla\phi + \tilde{\boldsymbol{v}}$, where $(\nabla \cdot \tilde{\boldsymbol{v}}) = 0$ and ϕ is a potential. Then, introducing two-dimensional stream function for $\tilde{\boldsymbol{v}}$, the transverse velocity components are presented in the form

$$v_r = \frac{\partial \phi}{\partial r} + \frac{1}{r} \frac{\partial \psi}{\partial \varphi}, \qquad v_\varphi = \frac{1}{r} \frac{\partial \phi}{\partial \varphi} - \frac{\partial \psi}{\partial r} \tag{10}$$

Let us introduce the axial vorticity

$$\Omega = \frac{1}{r} \left(\frac{\partial (r v_\varphi)}{\partial r} - \frac{\partial v_r}{\partial \varphi} \right)$$

The equations determining ϕ, ψ, and Ω are

$$\Delta \phi = -W \tag{11}$$

$$\Delta \psi = -\Omega \tag{12}$$

$$(\boldsymbol{v} \cdot \nabla)\Omega - W\Omega = Re^{-1} \Delta \Omega \tag{13}$$

whereas Eq. (4) determining W remains unchanged.

For the boundary conditions at the chamber surface we require that the wall-normal injection velocity condition is satisfied by the potential part of the velocity, $(\nabla\phi \cdot \boldsymbol{n})|_{r=R} = 1$, or

$$\left(\frac{\partial \phi}{\partial r} - \frac{R^I}{R^2} \frac{\partial \phi}{\partial \varphi} \right) \Bigg|_{r=R} = -\sqrt{1 + (R^I/R)^2} \tag{14}$$

The solenoidal part of the velocity field satisfies the condition

$$\left(\frac{\partial\psi}{\partial\varphi}+R^{I}\frac{\partial\psi}{\partial r}\right)\bigg|_{r=R}\equiv\frac{\mathrm{d}\psi}{\mathrm{d}\varphi}\bigg|_{r=R}=0$$

indicating that the stream function takes a constant value, say zero, on the chamber wall,

$$\psi|_{r=R}=0 \tag{15}$$

Handling the tangential velocity condition gives

$$\frac{\partial\psi}{\partial r}\bigg|_{r=R}=\frac{1}{R[1+(R^{I}/R)^{2}]}\frac{\mathrm{d}\phi}{\mathrm{d}\varphi}\bigg|_{r=R} \tag{16}$$

where $\mathrm{d}\phi/\mathrm{d}\varphi|_{r=R}=(R^{I}\partial\phi/\partial r+\partial\phi/\partial\varphi)|_{r=R}$. The symmetry conditions (7) read

$$\varphi=0\quad\text{and}\quad\varphi=\alpha/2\text{:}\ \frac{\partial\phi}{\partial\varphi}=\frac{\partial W}{\partial\varphi}=\psi=\Omega=0 \tag{17}$$

and all functions remain finite at $r\to 0$.

IV. Numerical Solutions

Numerical studies presented in the paper were carried out for two kinds of chamber shapes, both given by

$$R=A\{1+b\cos(k\varphi)\},\qquad 0<\varphi<\alpha/2=\pi/N \tag{18}$$

In the first case $k=N$ was employed, leading to a smooth shape of the chamber cross section. In the second case we use the values of k less then N, for which Eq. (18) describes the shapes with a nonsmooth corner at $\varphi=\alpha/2$. Parameter A was used in all cases to normalize the cross section perimeter requiring $\int_0^{\alpha/2}\sqrt{R^2+R^{I2}}\,\mathrm{d}\varphi=\pi/N$. The other parameter, b, is free and measures the deviation (not small in this study) of the shape from the circular one. In all cases presented in the paper $N=5$ was used.

For the purpose of facilitating the numerical analysis, the physical coordinate r is transformed into the computational coordinate η by means of the following relationship:

$$\eta=(r-r_m)/(R-r_m)$$

where r_m is a small value, say 10^{-3}, introduced to facilitate the boundary conditions at $r\ll 1$. Notice that in terms of η the computational domain is transformed into rectangular, $0<\eta<1$. Although the introduction of a coordinate mapping would appear to transform the governing equations to a rather complicated form, the approach is favored with a finite difference method applied in the study. The governing equations written in the transformed coordinates were solved numerically using a Gauss–Seidel iterations with overrelaxation for ϕ and ψ, and a pseudounsteady form for W and Ω. The mesh size was equi-spaced and sufficiently fine to provide the grid independence of the results.

A. Smooth Cross Section Area Shape

Consider first the chambers with the smooth cross section shape. Figure 2 shows, in the half of the sector, the streamlines defined by (8) and calculated with $b=0.1$, illustrating the changes in the flow structure with increasing values of the Reynolds number. We plot in this figure, with thick lines, two special streamlines. The first one has the origin, indicated by point a, at the chamber surface and separates the fluid directed to the chamber axis from the fluid tending to circulate outside the central part of the chamber.

Beginning with some critical value of the Reynolds number the vortex is formed in every half of the sector, as shown in Fig. 2 with cases $Re=500$ and $Re=1000$. Notice that the quantity of the fluid directed to the region of the chamber axis decreases with increasing values of Re and the most of the fluid tends to recirculate around these vortices. The critical value of Re depends on the geometric parameters. For lower values of the Reynolds number, represented in Fig. 2 with the case $Re=100$, the vortex structure is not formed yet

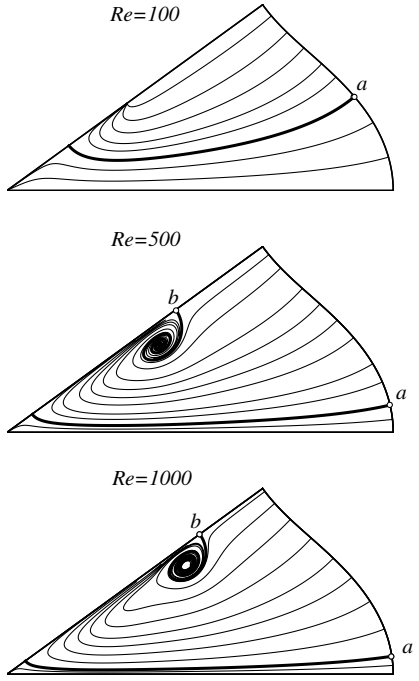

Fig. 2 Streamlines, calculated for various Reynolds numbers, $b=0.1$, and the smooth shape. Dividing streamlines are plotted with thick lines.

and the fluid which is not directed to the chamber axis tends to the axis of symmetry, $\varphi=\alpha/2$, between two halves of the sector.

The second special streamline, plotted in Fig. 2 with thick lines for $Re=500$ and 1000, has the origin, indicated by b, at the line of symmetry $\varphi=\alpha/2$, whereas the other streamlines originate at the chamber surface. This streamline acts as an attractor for all streamlines tending to the vortex, and therefore it does not appear for cases with the Reynolds number lower than a critical one. With increasing values of the Reynolds number the point b tends to approach the chamber surface. Figure 3 shows the examples of the isolines of the axial velocity gradient W and the isolines of the axial vorticity Ω.

With increasing values of b corresponding to more noncircular shapes, the threshold value of Re above which the vortex structure is formed decreases. Shown in Fig. 4 are the streamlines calculated with $b=0.3$. Observe the existence of the vortex for $Re=100$ and also the beginning of formation of the secondary vortex for $Re=2000$. Shown in Fig. 5 are the isolines of axial vorticity and the axial velocity gradient plotted for the same values of the Reynolds number.

To compare the structure of the flows near the vortex for different Re we plot, in Fig. 6, the isolines of the vorticity Ω and the velocity

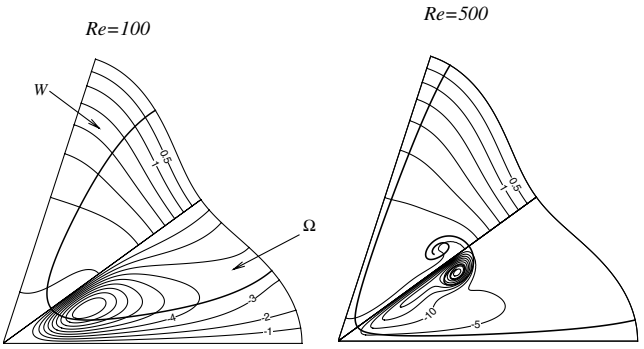

Fig. 3 Isolines of the axial vorticity (lower halves of the sectors, Ω at intervals of 1 for $Re=100$ and 5 for $Re=500$) and the axial velocity gradient (upper halves of the sectors, W at intervals of 0.5) computed for $b=0.1$ and the smooth cross section shape. Dividing streamlines are shown with thick lines.

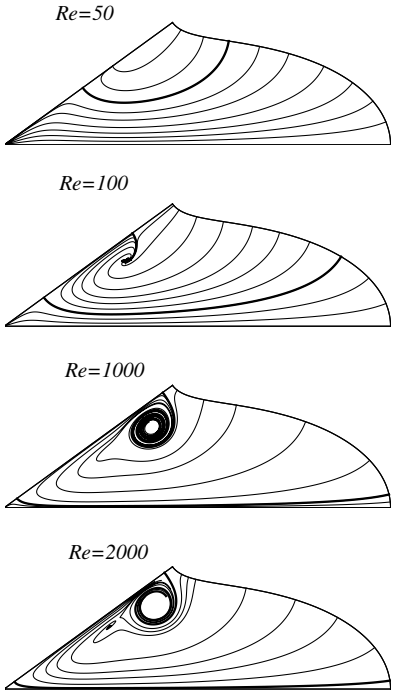

Fig. 4 Streamlines calculated for $b = 0.3$ and various Reynolds numbers. Dividing streamlines are shown with thick lines.

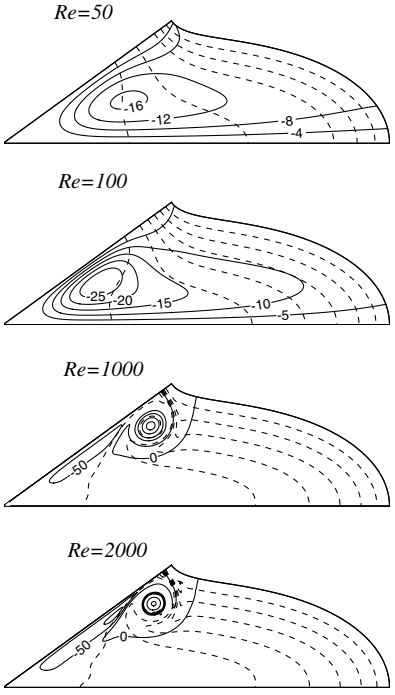

Fig. 5 Isolines of W (dashed lines, W at intervals of 1) and isolines of Ω (solid lines) calculated for $b = 0.3$ and various Reynolds numbers. Isolines of Ω without labels are $-300, -200, -100, -50$ for $Re = 1000$, and $-1000, -500, -100, -50$ for $Re = 2000$.

gradient W calculated with $b = 0.3$ for $Re = 200$ and 400 showing also the dividing streamlines. One can see clearly in this figure that there is a distance between the point of the maximum absolute value of the vorticity (the vorticity is negative in the most part of this half of the sector) and the center of the vortex. This distance decreases with increasing of Re. One can see also that the variation of W in the neighborhood of the vortex is weak. These observations are used in Sec. V to describe asymptotically the flow near the vortex. Notice the appearance of the region of the positive vorticity, plotted with dashed

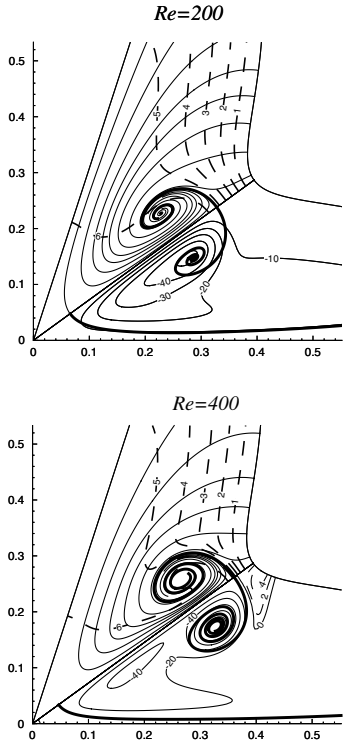

Fig. 6 Isolines of the axial vorticity in the lower half of the sectors (negative levels of Ω at intervals of 10 for $Re = 200$ and at intervals of 20 for $Re = 400$ plotted with solid lines; the positive levels for $Re = 400$ are plotted at intervals of 2 with dashed lines) and the axial velocity gradient in the upper half of the sectors (plotted with dashed lines at intervals of 1). Streamlines are plotted with thin solid lines and dividing streamlines are shown with thick lines.

lines, and pronounced formation of the shear layer near the dividing streamline for $Re = 400$.

B. Nonsmooth Cross Section Area Shape

Illustrating the influence of the nonsmooth corner in the cross section shape on the flowfield structure we plot, in Fig. 7, the isolines of the vorticity Ω and the velocity gradient W calculated for $Re = 200$ and $k = 4$. In this case the angle β between the solid surface and the axis of symmetry, as indicated in Fig. 7, is $\beta \approx 133$ deg (in the smooth case $\beta = 90$ deg). This figure can be compared with Fig. 6 where the case with $Re = 200$ and the smooth shape has been plotted. The presence of the nonsmooth corner leads to the singular behavior of the vorticity field near the corner.

Let us use the local cylindrical coordinates $(\hat{r}, \hat{\varphi})$ attached to the corner as shown in Fig. 8. For values $\hat{r} \ll Re^{-1}$ the flow is described,

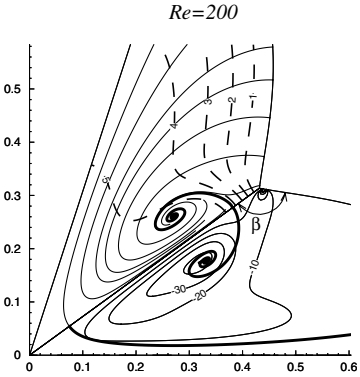

Fig. 7 Case of the nonsmooth cross section shape for $Re = 200$. Upper half of the sector: axial velocity gradient W (dashed lines) and streamlines (thin solid lines); lower half of the sector: isolines of the axial vorticity Ω (thin solid lines) and dividing streamlines (thick solid lines).

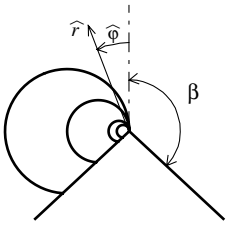

Fig. 8 Sketch of the local cylindrical coordinates near the corner and the isolines of (22).

in first approximation, by the Stokes equations

$$\hat{\Delta}^2\psi = 0, \qquad \hat{\Delta}\phi = -W, \qquad \hat{\Delta}W = 0 \tag{19}$$

where $\hat{\Delta}$ denotes the operator written in terms of local coordinates. They are to be solved with the conditions

$$\hat{\varphi} = \beta\text{: } \hat{r}^{-1}\partial\phi/\partial\hat{\varphi} = -1, \qquad \psi = W = \hat{r}^{-1}\partial\psi/\partial\hat{\varphi} + \partial\phi/\partial\hat{r} = 0$$
$$\hat{\varphi} = 0\text{: } \partial\phi/\partial\hat{\varphi} = \partial\phi/\partial W = \psi = \partial^2\psi/\partial\hat{\varphi}^2 = 0 \tag{20}$$

The leading terms of the solution are

$$\psi = -\hat{r}\frac{(\beta\cos\beta\sin\hat{\varphi} - \hat{\varphi}\cos\hat{\varphi}\sin\beta)\cos\beta}{(\beta - \sin\beta\cos\beta)\sin\beta}, \qquad \phi = \hat{r}\frac{\cos\hat{\varphi}}{\sin\beta}$$
$$W = B_1\hat{r}^{\pi/2\beta}\cos(\pi\hat{\varphi}/2\beta) \tag{21}$$

where B_1 is a constant that cannot be determined by purely local considerations. The leading term of the vorticity expansion near the corner becomes

$$\Omega = \frac{2\cos\beta}{\beta - \sin\beta\cos\beta}\frac{\sin\hat{\varphi}}{\hat{r}} \tag{22}$$

Observe, that the singularity given by (22) disappears for $\beta \to 90$ deg. The isolines of (22) are shown in Fig. 8 in one half of the sector. They resemble, qualitatively, those near the corner, shown in Fig. 7, taking into account that in the numerical calculations using the finite difference method the vorticity values remain finite at all grid points. Fortunately, this singularity remains to be local and does not affect much the flow far from the corner, as in many studies carried out for cases with similar nonsmooth geometries.

C. Evaluation of the Constant *C*

Our interest lies in the numerical evaluation of the constant C appearing in (1), and determining the axial pressure gradient as a function of the Reynolds number. The results are plotted in Fig. 9 for various cross sections. One can see that this value varies weakly with the Reynolds number at $Re \gg 1$ resembling the results obtained in [1] for the circular cross section.

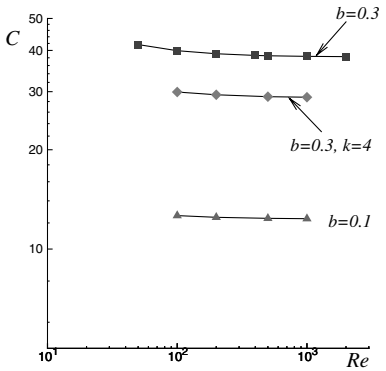

Fig. 9 Calculated values of the constant *C* vs *Re* for various cross section shapes.

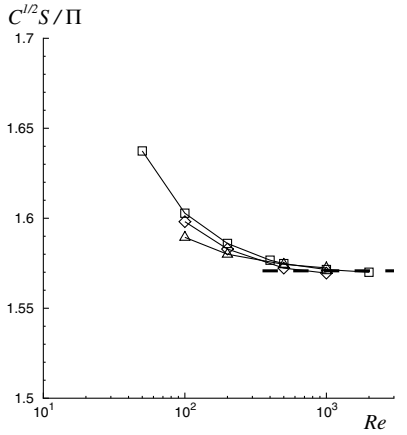

Fig. 10 Calculated values of $C^{1/2}S/\Pi$ as functions of Reynolds number. Value of $\pi/2$ provided by the Culick's solution is shown with a dashed line.

In contrast, the numerical value of C results very sensitive to the geometric parameters b and k. In the present study the length scale r_c has been used such that the nondimension perimeter of the cross section area, Π, is equal to 2π. The nondimension cross section area itself, $S = (1/2)\int_0^{2\pi} R^2\,\mathrm{d}\varphi$, depends on geometry leading to the appreciable variations of C shown in Fig. 9.

Nevertheless, we find unexpectedly weak dependence on b and k, say the geometry, for the value $C^{1/2}S/\Pi$ plotted in Fig. 10, where we give also, with a dashed line, the value $\pi/2$ provided by the Culick's solution [5]. Observe, that the variations of $C^{1/2}S/\Pi$ are less than 1% beginning with $Re = 100$ for all configurations considered.

It is easily seen that $C^{1/2}S/\Pi$ is invariable with the transformation of the length scale. Indeed, if the new length scale is $\tilde{l} = ml$, where l is the old one, then $\tilde{C} = Cm^2$, $\tilde{S} = S/m^2$, and $\tilde{\Pi} = \Pi/m$. Equation (4) written in the inviscid limit, $(\boldsymbol{v}\cdot\nabla)W = C - W^2$, has the formal solution

$$W = C^{1/2}\tanh\left\{C^{1/2}\int_0^s \frac{\mathrm{d}s}{v_s}\right\} \tag{23}$$

where the integration is carried out along a streamline. One can see that W grows along the streamline, beginning with the zeroth value at the propellant surface, $s = 0$, toward the maximum value $W_{\max} = C^{1/2}$, at $s \to \infty$. It is assumed here that there exists a streamline along which the integral in the right-hand side of (23) goes to infinity as $s \to \infty$. From the continuity equation it follows that $\bar{W}S = \Pi$, where $\bar{W}$ is the mean value of W. Then, the value $C^{1/2}S/\Pi$ approaches $W_{\max}/\bar{W}$ at $Re \gg 1$.

In the case of the planar counterpart of the Culick [5] solution,

$$\tilde{v} = -\sin\left(\tfrac{1}{2}\pi y\right), \qquad \tilde{w} = \tfrac{1}{2}\pi\cos\left(\tfrac{1}{2}\pi y\right), \qquad C = \tfrac{1}{4}\pi^2$$
$$-1 < y < 1$$

the value of $C^{1/2}S/\Pi$ is also equal to $\pi/2$, where $S = 2$ and $\Pi = 2$ for the unit transverse length.

We hazard a conjecture that $C^{1/2}S/\Pi = \pi/2$ for any closed slender cavities in the invicsid limit. To provide support for this, the steady flows described by (4) and (11–13) were calculated numerically in the rectangular cavities for various values of the aspect ratio. The evolution of the flow structure in the rectangular cavity with increasing values of Re or changing the aspect ratio is interesting, but will not be analyzed in this paper. We give only, in Fig. 11, in a quarter of square, the streamlines calculated with various Re, and in Fig. 12, the isolines of Ω and W calculated for $Re = 1000$. Table 1 shows the calculated values of $C^{1/2}S/\Pi$. One can see that, despite complicated structure of flows shown in Figs. 11 and 12, the value of $C^{1/2}S/\Pi$ approaches $\pi/2$ and the differences between the calculated values and $\pi/2 \approx 1.571$ are of order $1/Re$.

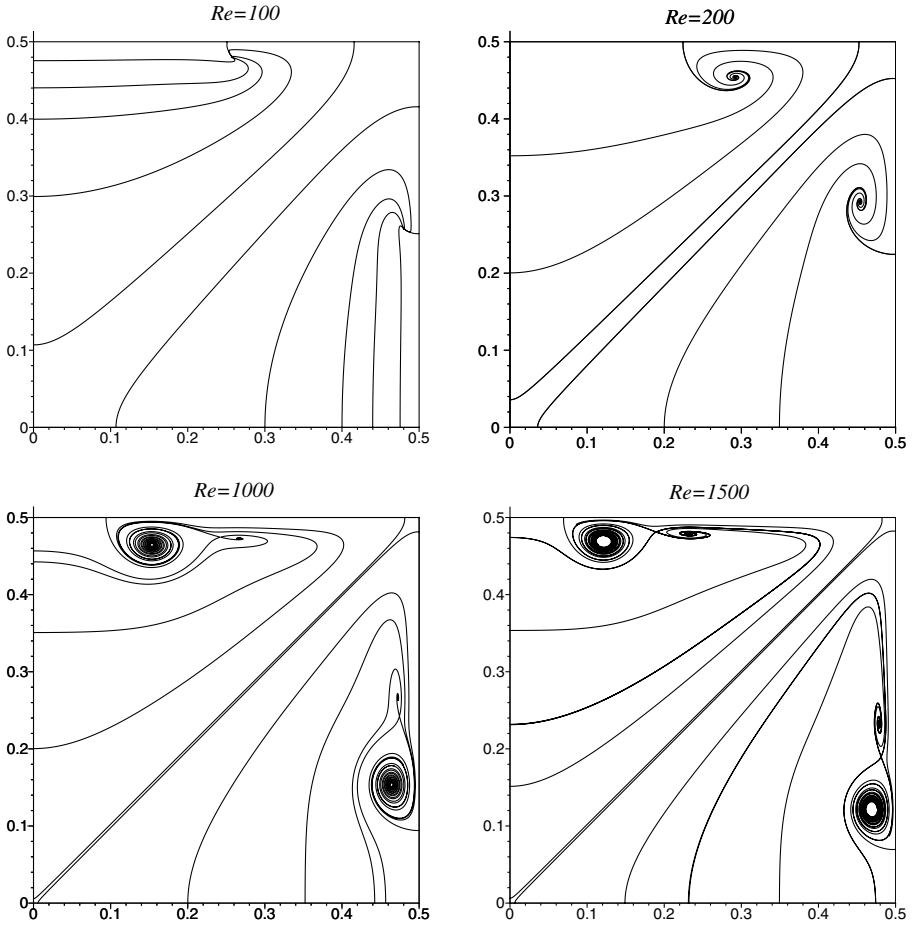

Fig. 11 Streamlines calculated in the square domain for various Reynolds numbers.

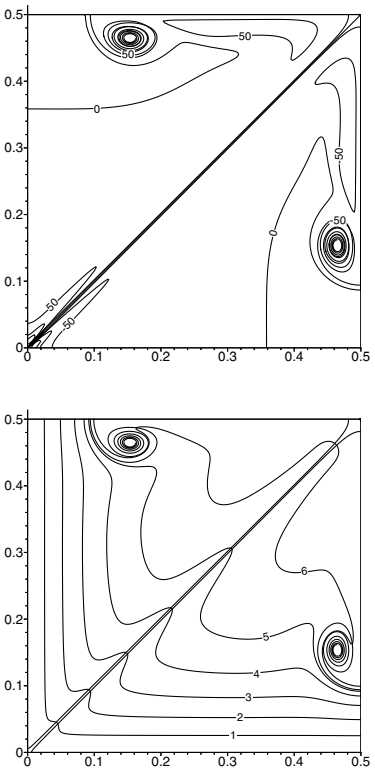

Fig. 12 Isolines of the axial vorticity Ω (upper plot) and the axial velocity gradient W (lower plot) calculated for $Re = 1000$ in the square domain.

V. Asymptotic Solution Near the Vortex

We shall describe in this section the asymptotic behavior of the flowfield near the vortex at large Reynolds numbers. The preceding numerical results showed that in this region the vorticity has a peak Ω_m (negative in this half of the sector) growing as Re. For example, the numerical calculations carried out with $b = 0.1$ give $\Omega_m = -9.97$ for $Re = 100$ and $\Omega_m = -101.3$ for $Re = 1000$. From the other side, the variations of W are weak in this region.

Let us place the origin of the local cylindrical coordinates $(\tilde{r}, \varphi)$ in the point of the maximum absolute value of the vorticity. Introducing the stretched inner variable $\xi = Re^{1/2}\tilde{r}$, assumed to be of order unity in the viscous core, the asymptotic solution is sought in the following form:

$$\begin{aligned} \psi &= \psi_0(\xi) + Re^{-1/2}\psi_1(\xi,\varphi) + Re^{-1}\psi_2(\xi,\varphi) + \cdots \\ \Omega &= Re\,\Omega_0(\xi) + Re^{1/2}\Omega_1(\xi,\varphi) + \Omega_2(\xi,\varphi) + \cdots \\ W &= W_0(\xi) + Re^{-1/2}W_1(\xi,\varphi) + Re^{-1}W_2(\xi,\varphi) + \cdots \\ \phi &= Re^{-1}\phi_0(\xi) + Re^{-3/2}\phi_1(\xi,\varphi) + Re^{-2}\phi_2(\xi,\varphi) + \cdots \end{aligned} \tag{24}$$

anticipating that the leading terms in (24) are functions of ξ only. Substituting (24) into equations for W and ϕ, rewritten in terms of ξ, and equating the same order in Re terms provides

$$\frac{1}{\xi}\frac{\partial\psi_1}{\partial\varphi}\frac{\mathrm{d}W_0}{\mathrm{d}\xi} = 0, \qquad \frac{1}{\xi}\frac{\mathrm{d}}{\mathrm{d}\xi}\left(\xi\frac{\mathrm{d}\phi_0}{\mathrm{d}\xi}\right) = -W_0 \tag{25}$$

Then, W_0 takes a constant value, say $W_0 = w_c$, and $\phi_0 = -w_c\xi^2/4$.

Substituting (24) into the corresponding equations for ψ and Ω gives

Table 1 Computed values of $C^{1/2}S/\Pi$ in rectangular cavities for various Reynolds numbers and aspect ratios

Re	1:1	1:2	1:3
500	1.577	1.575	1.574
100	1.605	1.596	1.594
200	1.588	1.583	1.581
1000	1.573	1.572	——
1500	1.572	——	——

$$\frac{1}{\xi}\frac{\mathrm{d}}{\mathrm{d}\xi}\left(\xi\frac{\mathrm{d}\psi_0}{\mathrm{d}\xi}\right)=-\Omega_0 \tag{26}$$

$$\frac{1}{\xi}\frac{\partial}{\partial\xi}\left(\xi\frac{\partial\psi_1}{\partial\xi}\right)+\frac{1}{\xi^2}\frac{\partial^2\psi_1}{\partial\varphi^2}=-\Omega_1 \tag{27}$$

$$\frac{\mathrm{d}\Omega_0}{\mathrm{d}\xi}\frac{\partial\psi_1}{\partial\varphi}-\frac{\mathrm{d}\psi_0}{\mathrm{d}\xi}\frac{\partial\Omega_1}{\partial\varphi}=0 \tag{28}$$

$$\frac{\mathrm{d}\Omega_0}{\mathrm{d}\xi}\frac{\partial\psi_2}{\partial\varphi}-\frac{\mathrm{d}\psi_0}{\mathrm{d}\xi}\frac{\partial\Omega_2}{\partial\varphi}+\frac{\partial\Omega_1}{\partial\xi}\frac{\partial\psi_1}{\partial\varphi}-\frac{\partial\psi_1}{\partial\xi}\frac{\partial\Omega_1}{\partial\varphi}=\frac{1}{\xi}\frac{\mathrm{d}}{\mathrm{d}\xi}\left(\xi\frac{\mathrm{d}\Omega_0}{\mathrm{d}\xi}\right)+\frac{1}{2}w_c\xi\frac{\mathrm{d}\Omega_0}{\mathrm{d}\xi}+w_c\Omega_0 \tag{29}$$

From (28) it follows that $\Omega_1=K(\xi)\psi_1+M(\xi)$, where $K(\xi)=(\mathrm{d}\Omega_0/\mathrm{d}\xi)/(\mathrm{d}\psi_0/\mathrm{d}\xi)$ and $M(\xi)$ are functions of ξ only. When (29) integrated over φ from 0 to 2π, the periodicity leads to

$$\int_0^{2\pi}\left(\frac{\mathrm{d}\Omega_0}{\mathrm{d}\xi}\frac{\partial\psi_2}{\partial\varphi}-\frac{\mathrm{d}\psi_0}{\mathrm{d}\xi}\frac{\partial\Omega_2}{\partial\varphi}\right)\mathrm{d}\varphi=0$$

For the others terms in the left-hand side of (29) one can obtain

$$\int_0^{2\pi}\left(\frac{\partial\Omega_1}{\partial\xi}\frac{\partial\psi_1}{\partial\varphi}-\frac{\partial\psi_1}{\partial\xi}\frac{\partial\Omega_1}{\partial\varphi}\right)\mathrm{d}\varphi=-\int_0^{2\pi}\left(\psi_1\frac{\partial^2\Omega_1}{\partial\xi\partial\varphi}-\Omega_1\frac{\partial^2\psi_1}{\partial\xi\partial\varphi}\right)\mathrm{d}\varphi=-\int_0^{2\pi}\left(K'\psi_1\frac{\partial\psi_1}{\partial\varphi}-M\frac{\partial^2\psi_1}{\partial\xi\partial\varphi}\right)\mathrm{d}\varphi$$
$$=\left(-\frac{1}{2}K'\psi_1^2-M\frac{\partial\psi_1}{\partial\xi}\right)\Big|_0^{2\pi}=0$$

Hence, the solvability condition of (29) is

$$\frac{1}{\xi}\frac{\mathrm{d}}{\mathrm{d}\xi}\left(\xi\frac{\mathrm{d}\Omega_0}{\mathrm{d}\xi}\right)+\frac{1}{2}w_c\xi\frac{\mathrm{d}\Omega_0}{\mathrm{d}\xi}+w_c\Omega_0=0 \tag{30}$$

The solutions for Ω_0 and ψ_0 take the form

$$\Omega_0=C_1\exp(-w_c\xi^2/4),\qquad \psi_0=C_1w_c^{-1}[-2\,\ell_n(\xi)-\mathrm{Ei}(w_c\xi^2/4)] \tag{31}$$

where the part singular at $\xi=0$ has been eliminated. Here $\mathrm{Ei}(z)=\int_1^\infty\mu^{-1}\exp(-z\mu)\,\mathrm{d}\mu$ denotes the exponential integral and C_1 is a constant that can be determined by the matching with the outer numerical solution. In particular for $b=0.1$ and the smooth cross section shape $C_1\approx-0.1$.

The solution of (27) and (28) takes the form

$$\psi_1=\sum_{n=1}^{\infty}b_nf_n(\xi)\cos[n(\varphi-\varphi_0)] \tag{32}$$

where the phase φ_0 and the coefficients b_n again are determined by the matching with the outer solution. The functions f_n satisfy the equations

$$f_n''+\frac{1}{\xi}f_n'-\left[\frac{n^2}{\xi^2}+\frac{1}{4}\xi^2w_c^2\frac{\exp(-w_c\xi^2/4)}{\exp(-w_c\xi^2/4)-1}\right]f_n=0 \tag{33}$$

The analytic solution for $n=1$ is

$$f_1(\xi)=\xi^{-1}[\exp(-w_c\xi^2/4)-1] \tag{34}$$

where we have eliminated the singular at $\xi=0$ part. The solutions for $n>1$ can be obtained numerically. One can show that $f_n\sim\xi^n$ at $\xi\to0$.

Two terms of the velocity expansion written in terms of the unstretched variables become

$$v_r=-\frac{w_c\tilde r}{2}-b_1\frac{e^{-w_cRe\tilde r^2/4}-1}{Re\tilde r^2}\sin(\varphi-\varphi_0)$$
$$v_\varphi=-2C_1\frac{e^{-w_cRe\tilde r^2/4}-1}{w_c\tilde r}+b_1\left(\frac{1}{2}w_ce^{-w_cRe\tilde r^2/4}+\frac{e^{-w_cRe\tilde r^2/4}-1}{Re\tilde r^2}\right)\cos(\varphi-\varphi_0) \tag{35}$$

In particular at $\tilde r=0$ the velocity becomes

$$v_r=\frac{1}{4}b_1w_c\sin(\varphi-\varphi_0),\qquad v_\varphi=\frac{1}{4}b_1w_c\cos(\varphi-\varphi_0) \tag{36}$$

One can see that the point of the maximum absolute value of the vorticity, $\tilde r=0$, does not coincide with the center of the vortex, where $v_r=v_\varphi=0$, at finite values of Re. The distance between these points decreases as $Re^{-1/2}$ with increasing values of the Reynolds number.

VI. Conclusions

The main objective of the paper is the study of flows in slender nonaxisymmetric cavities of solid propellant rockets. The slenderness permits to reduce the problem to the calculations of the self-similar solution which describes the flow far enough from the end wall of the cavity. The cross section of the cavity is assumed to be noncircular and the calculations of the steady flows were carried out in the half of the sector, $0<\varphi<\pi/N$, where N is the number of sectors.

The numerical results of the present paper are in agreement with the conclusion given in Balachandar et al. that even modest deviations from axial symmetry cause the vortexes with large values of the axial vorticity. At large Reynolds numbers, we give in the paper the asymptotic solution near the center of the vortex where the inviscid solution failures. It has been shown that the value of the axial vorticity becomes of order of Reynolds number in the viscous core. These vortexes are encountered outside the neighborhood of the centerline of the camber, due to nonsmall deviations of the cross section shape from axial symmetry.

The self-similar form of the solution includes the constant C, unknown a priori, which determines the pressure distribution along the cavity axis. It was well founded expectation that this value varies weakly at large Reynolds numbers, precisely the variations decay as $1/Re$, and it has been confirmed numerically for various shapes. Nevertheless, it was an unexpected revelation to find that one property of the flow, namely, $C^{1/2}S/\Pi$, is practically independent on the cross section geometry at $Re\gg1$. It approaches to $\pi/2$, the value provided by both the inviscid Culick's solution [5] for the circular cross section and its planar counterpart. The discrepancy found between the numerical values of $C^{1/2}S/\Pi$ and $\pi/2$ is less than 1% for $Re>100$. It can be supposed that $C^{1/2}S/\Pi=\pi/2$ in the inviscid limit for any cross section, a conjecture that obtained also a numerical support in cases of the rectangular cavities. Its rigorous proof based on the analysis of the Euler equations looks complicated and remains unknown for the author.

Acknowledgments

The author acknowledges the financial support received from the Spanish Government through the Ramon y Cajal Program. The author would also like to express his gratitude to Amable Liñán of Universidad Politécnica de Madrid for continuing advice and counsel on this work.

References

[1] Balachandar, S., Buckmaster, J. D., and Short, M., "The Generation of Axial Vorticity in Solid-Propellant Rocket-Motor Flows," *Journal of Fluid Mechanics*, Vol. 429, 2001, pp. 283–305.

[2] Berman, A. S., "Laminar Flow in Channels with Porous Walls," *Journal of Applied Physics*, Vol. 24, No. 9, 1953, 1232–1235.

[3] Taylor, G. I., "Fluid Flow in Regions Bounded by Porous Surfaces," *Proceedings of the Royal Society of London A*, Vol. 234, No. 1199, 1956, pp. 456–475.

[4] Proudman, I., "An Example of Steady Flow at Large Reynolds Number," *Journal of Fluid Mechanics* Vol. 9, 1960, pp. 593–602.

[5] Culick, F. E. C., "Rotational Axisymmetric Mean Flow and Damping of Acoustic Waves in Solid Propellant Rocket Motors," *AIAA Journal*, Vol. 4, No. 8, 1966, pp. 1462–1464.

[6] Balacrishnan, G., Liñán, A., and Williams, F. A., "Rotational Inviscid Flow in Laterally Burning Solid Propellant Rocket Motors," *Journal of Propulsion and Power*, Vol. 8, No. 6, 1992, pp. 1167–1176.

[7] Dunlap, R., Willoughby, P. G., and Hermsen, R. W., "Flow Field in the Combustion Chamber of a Solid Propellant Motor," *AIAA Journal*, Vol. 12, No. 10, 1974, pp. 1400–1441

[8] Majdalani, J., Vyas, A. B., and Flandro, G. A., "Higher Mean-Flow Approximation for Solid Rocket Motors with Radially Regressing Walls," *AIAA Journal*, Vol. 40, No. 9, 2002, 1780–1788.

[9] Dauenhauer, E. C., and Majdalani, J., "Exact Self-Similarity Solution of the Navier–Stokes Equations for a Porous Channel with Orthogonally Moving Walls," *Physics of Fluids*, Vol. 15, No. 6, 2003, pp. 1485–1495.

[10] Griffond, J., Casalis, G., and Pineau, J.-P., "Spatial Instability of Flow in a Semiinfinite Cylinder with Fluid Injection Through Its Porous Walls," *European Journal of Mechanics B, Fluids*, Vol. 19, No. 1, 2000, pp. 69–87.

[11] Griffond, J., and Casalis, G., "On the Nonparallel Stability of the Injection Induced Two-Dimensional Taylor Flow," *Physics of Fluids*, Vol. 13, No. 6, 2001, pp. 1635–1644.

[12] Chedevergne, F., Casalis, G., and Féraille. T., "Biglobal Linear Stability Analysis of the Flow Induced by Wall Injection," *Physics of Fluids*, Vol. 18, No. 1, 2006, p. 014103.

[13] Sutton, G. P., and Biblarz, O., *Rocket Propulsion Elements*, John Wiley & Sons, New York, 2001.

[14] Liñán, A., Kurdyumov, V., and Soler, J., "The Flow Field in the Slender Combustion Chambers of Solid Propellant Rockets," *Simplicity, Rigor and Relevance in Fluid Mechanics*, CIMNE, Barcelona, 2004, pp. 127–140.

S. Aggarwal
Associate Editor